Article

Fabrication and Luminescent Properties of Zn–Cu–In–S/ZnS Quantum Dot Films under UV Excitation

G. Saatsakis [1] **, C. Michail** [2] **, C. Fountzoula** [3] **, N. Kalyvas** [2] **, A. Bakas** [3] **, K. Ninos** [3] **, G. Fountos** [2] **, I. Sianoudis** [3] **, I. Kandarakis** [2] **, G.S. Panayiotakis** [1] **and I. Valais** [2,*]

[1] Department of Medical Physics, School of Medicine, University of Patras, GR-15310 Rion, Greece; gsaatsakis@upatras.gr (G.S.); panayiot@upatras.gr (G.S.P.)
[2] Radiation Physics, Materials Technology, and Biomedical Imaging Laboratory, Department of Biomedical Engineering, University of West Attica, 122 10 Athens, Greece; michail@upatras.gr (C.M.); nkalyvas@uniwa.gr (N.K.); gfoun@uniwa.gr (G.F.); kandarakis@uniwa.gr (I.K.)
[3] School of Biomedical Sciences, University of West Attica, 122 10 Athens, Greece; chfountz@uniwa.gr (C.F.); abakas@uniwa.gr (A.B.); kninos@uniwa.gr (K.N.); jansian@uniwa.gr (I.S.)
* Correspondence: valais@uniwa.gr; Tel.: +30-210-5385-371

check for updates

Abstract: Quantum dots (QDs) are quite interesting materials due to their unique chemical and physical properties. ZnCuInS/ZnS QDs can be produced either in hydrophobic or hydrophilic form, are non-toxic, and thus favorable for studies in the area of biology. Poly(methyl methacrylate) (PMMA) is a well-known biocompatible resin which is widely used in dentistry, ophthalmology, and orthopedic surgery. Four composite PMMA films of ZnCuInS/ZnS nanocrystals with maximum emission at 530 nm and concentrations of 1.0, 4.0, 6.0, and 10.0 %*w/v*, were prepared. X-ray irradiation was used to evaluate the volume homogeneity of the final samples, as a measure of QD dispersion. The luminescent efficiency was evaluated, under ultraviolet (UV) irradiation. The process of UV irradiation involved the experimental measurement of the forward luminescent light, as well as the backward luminescent light, in order to accurately calculate the energy quantum efficiency (EQE) of ZnCuInS/ZnS QDs. Reflected UV radiation was also measured, and results showed that it ranges from 2% to 6% approximately as the QD concentration rises from 1.0 %*w/v* to 10.0 %*w/v*. Beyond 6.0 %*w/v*, the reflected UV radiation remains essentially unchanged. Additionally, the reflected UV radiation remained unaffected as the power of the incident UV increased. Approximately 9% of incident UV radiation passed through the 1.0 %*w/v* sample, whereas for the samples with higher ZnCuInS/ZnS concentration, 0% UV radiation passed through. The EQE reached a maximum of about 45% with the 10.0 %*w/v* sample, while it remained practically unaffected relative to the increase of the emitted UV power. The homogeneity measurements revealed that the coefficient of variation (CV) increased with increasing concentration, for the 1.0, 4.0, and 6.0 %*w/v* samples. The minimum CV was obtained for the sample of 10.0 %*w/v* due to the incorporation of sonication in the final product, during the fabrication process.

Keywords: quantum dots; ZnCuInS/ZnS; UV; energy quantum efficiency; polymer film

1. Introduction

Quantum dots (QDs) are inorganic semiconductor nanocrystals with sizes in the nanoscale range [1]. The size, shape, and consequently the number of electrons they contain can be accurately controlled by chemical processes [2]. During fluorescence stimulation, quantum dots are excited by radiation of specific energy and emit in different wavelengths, depending on their size [3–5]. Their

excellent chemical and physical properties, such as the high energy conversion efficiency, the high extinction coefficient, tunable emitting wavelength, the broad excitation spectrum, and the resistance to photobleaching have attracted the interest of the scientific community providing quite impressive results [6–12]. QDs are 20 times brighter and 100 times more stable than traditional fluorescent indicators [13]. In the area of biology, because of their microscopic size and high penetrating ability, they can enter tissue and cells with ease. QDs make the long-term real-time monitoring and tracking of molecules and cells more feasible. During the last years, QDs have been employed in many areas such as solar cells, transistors, light-emitting diodes (LEDs), medicine and biology applications, as well as in quantum computing [14–22]. QDs that contain cadmium or mercury have been used in the above areas; however, for biomedical applications, QDs must meet additional criteria since toxic compounds are not allowed. High toxicity in the biological environment can destroy cells and tissues. European Union Directive 2011/65/EU "Restriction of the use of certain hazardous substances" (RoHS) [23] has set the limits of hazardous toxic compounds, such as cadmium or mercury, to protect humans as well as the environment. Under the prism of nontoxicity, cadmium-free ZnCuInS/ZnS QDs might be an interesting candidate for medical applications. Another important factor which dictated the use of ZnCuInS/ZnS QDs was the fact that they emit light in the green region of the optical spectrum, being compatible with the most common digital optical sensors that are utilized in biomedical instrumentation [24–28]. Multiple methods have been reported for the preparation of QD films [29–32]. Previous work of our group introduced a simple method for the fabrication of composite films using a mixture of powder scintillators and PMMA. PMMA is a well-known thermoplastic which is widely used in biomedical applications. [28,33–35]. The in vitro and in vivo biocompatibility of PMMA has been studied extensively, and its resins are broadly used in medicine [36]. In ophthalmology, intraocular lenses are made of PMMA, while in orthopedic surgery, PMMA is used as bone cement in joint replacements, screw fixation in bone, and filler for bone cavities and skull defects [36,37]. Furthermore, in dentistry PMMA is used in dental prostheses [38,39]. In this study, the luminescence efficiency of four ZnCuInS/ZnS/PMMA samples, prepared with the previously mentioned method, was evaluated for possible use in medical applications. Volume homogeneity as a measure of QD dispersion of the composite films was assessed using medical X-ray images.

2. Materials and Methods

PMMA (poly methyl methacrylate) powder (average Mw ~120,000 by gel permeation chromatography) and liquid MMA monomer were purchased from Sigma-Aldrich (St. Louis, MO, USA) and Alfa Aesar (Ward Hill, MA, USA), respectively, both with purities reaching 99%. PMMA and MMA were mixed in a ratio of 1:2.5 [35] in order to produce a slurry, with optimum viscosity for further handling and processing.

ZnCuInS/ZnS QDs (PL-QD-CF-530, particle size: 4–5 nm, emission wavelength: 530 ± 15 nm, cadmium free, hydrophobic) were purchased from PlasmaChem GmbH (Berlin, Germany), in powder form.

Different amounts of QDs (25, 100, 150, and 250 mg) were diluted in 1 mL toluene (Fluka Chemical, Milwaukee, WI, USA), with purity >99%. The dilution process was facilitated using an ultrasonic bath (TRITON—TR USR070) and a vortex (Velp Scientifica ZX3). Furthermore, 1.5 mL of the slurry PMMA/MMA was introduced into the QD solution, followed by vortex stirring. The final product of QD concentration 25, 100, and 150 mg was poured into flexible silicone molds, while the final product of QD concentration 250 mg underwent sonication for five minutes before it was poured into a flexible silicone mold too. Molds filled with the final products were put under vacuum for 15 min to remove entrapped air bubbles from the mixture. Removal of any residual solvent was accomplished by putting the samples in a vacuum oven (Vaciotem T, model 4001489) for 24 h at 50 °C.

The produced samples were labeled as QD25, QD100, QD150, and QD250, where the QD number indicates the amount of QD in milligrams within the sample (Table 1).

**Table 1.** Quantum dot (QD) concentrations along with their values in %*w/v*.

Ref.	mg QD/mL Toluene	%*w/v* in QD *
QD25	25	1.0
QD100	100	4.0
QD150	150	6.0
QD250	250	10.0

* In the final product, before molding.

Two experimental configurations were designed for the UV irradiation of the prepared films. Both involved the use of a UV source emitting at 365 nm (Prizmatix multichannel LED light source) and the forward and backward luminescent light was accurately measured by an integrating sphere (Ocean Optics Inc., Micropack Integrating Sphere 50 mm ISP-50-8-R-GT) followed by a grating optical spectrometer (Ocean Optics Inc., HR2000). Figure 1 shows the graphical representation of the forward and backward luminescence light, as well as the reflected and transmitted UV radiation. Measurements were fed into a laptop computer for presentation and further processing. Figure 2a,b shows the experimental configuration for the analysis of the forward luminescent light, as well as the incident UV radiation, that passes through the sample. As shown in Figure 2a, the UV irradiation originates from the UV source, is transmitted through a stabilized flexible optical fiber, and hits the compound film top surface perpendicularly. The distance between the sample and the optical fiber output orifice was carefully adjusted so that the visual pattern of the UV radiation accurately fit the input port orifice of the integrating sphere. Forward luminescent light produced by the sample, as well as the UV radiation that pass through the sample, was then collected by the integrating sphere. A slightly different experimental configuration was used in order to measure the reflected UV radiation, as well as the power of the backward luminescent light. In Figure 2b the output of the LED light source is driven through the optical fiber to the side input port of the integrating sphere. The light entering from the side input port of the integrating sphere is internally driven to hit the sample placed on the top sample port. The integrating sphere collects the backward luminescent light from the sample and the reflected UV radiation and feeds them to the optical spectrometer.
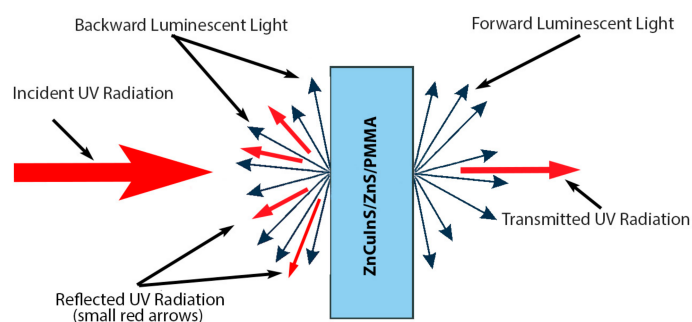
Figure 1. Graphical representation of the forward and backward luminescence light, as well as the reflected and transmitted UV radiation.
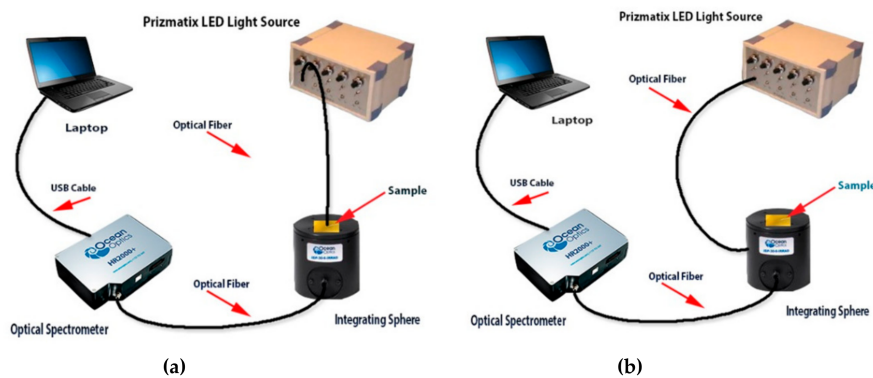
Figure 2. Experimental setups for the UV irradiation of the prepared films: (**a**) The experimental configuration for the measurement of the forward luminescent light produced by the sample, as well as the UV radiation that pass through the sample and (**b**) the experimental configuration for the measurement of the reflected UV, as well as the backward luminescent light produced by the sample.

All four compound films were irradiated with both the experimental configurations shown in Figure 2, to acquire the forward and backward luminescent light, as well as the reflected UV radiation. Additionally, the percentage of incident UV radiation that passed through the compound films was measured. Both the reflected UV radiation and the UV radiation that passed through the compound films should be subtracted from the incident UV radiation in order to accurately calculate the energy quantum efficiency (EQE). The intrinsic EQE of a scintillator is the ratio of photon energy emitted from the luminescent sites to the total energy trapped at those sites [40]. Disregarding any non-radiative relaxation processes, this ratio is:

$$\eta = \frac{E\lambda}{\beta Eg} \qquad (1)$$

where $E\lambda$ is the energy of emitted photons and Eg is the energy gap of the material. βEg is the total energy required for the creation of an electron–hole couple.

A Siemens Mammomat Inspiration was used to irradiate the four compound films in order to evaluate the volume homogenization in terms of QD dispersion. X-ray images were acquired using 32 KV and 8 mAs with total dose of 0.4807 mGy. Images were processed with the ImageJ software package to extract the coefficient of variation (CV) values of the samples. CV represents the ratio of the standard deviation to the mean, and it is a measure of the level of dispersion of data points in a data series around the mean.

$$cv = \frac{\sigma}{\mu} \qquad (2)$$

where σ is the sample standard deviation and μ is the sample mean.

3. Results

For this study, various UV irradiation intensities were used as shown in Figure 3a. Spectral presentation of the forward luminescent light for the QD250 sample is presented in Figure 3b.

Further analysis required the arithmetic measurement of the output UV radiation power. The Newport, ST 851-UV Power Meter was used, and the results are presented in Table 2.
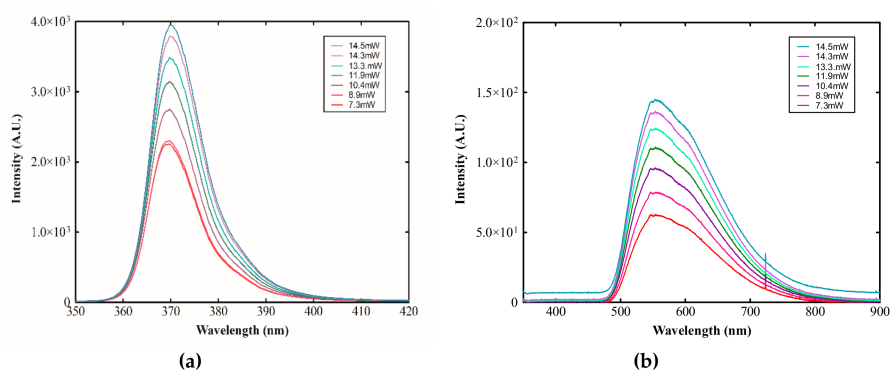
Figure 3. (**a**) Spectral presentation of the incident UV irradiation intensities and (**b**) spectral presentation of the forward luminescence of the QD250 when irradiated with the different incident UV intensities.

Table 2. Measurements of the output UV radiation power.

Power Steps	Output (mW)
1	7.3
2	8.9
3	10.4
4	11.9
5	13.3
6	14.3
7	14.5

Compound films were irradiated with X-rays in order to assess the volume homogeneity as a result of QD dispersion. Figure 4 shows the resulting images. Many QD aggregations are apparent in compound films QD100 and QD150. Since the fabrication process was the same for QD25, it is assumed that there are aggregations in that sample also, but they are not visible due to the small QD concentration. On the contrary, the sample with the highest QD concentration, QD250, has no visible aggregations which is attributed to the 5 min sonication which was added in the fabrication process. The CV was measured in each sample. Table 3 shows the CV measurements obtained using the ImageJ software package. The region of interest (ROI) was equal for all samples (area 139.414 square pixels). The CV value increased as the QD concentration increased while for the QD250 sample the CV value dropped dramatically due to the 5 min sonication incorporated in the fabrication method.
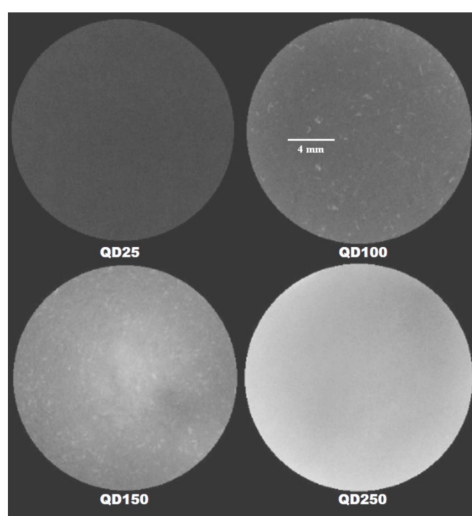
Figure 4. X-ray imaging of the four compound films.

Table 3. Coefficient of variation (CV) of the four ZnCuInS/ZnS/PMMA films.

| Concentration	Mean	SD	Min.	Max.	CV
25 mg	226.518	3.578	211.5	241.404	0.015796
100 mg	203.964	5.365	161.334	220.509	0.026304
150 mg	153.34	12.504	108.301	186.088	0.081544
250 mg	131.948	6.328	100.062	136.14	0.047958

Using the configuration described in Figure 2a, the forward luminescent light and the percentage of incident UV radiation that passed through the four compound films were measured, for the various steps of UV radiation power, as shown in Figure 5.

From Figure 5a, it can be deduced that in the examined UV energy range, the power of the forward luminescent light is linearly increased by increasing the power of the incident UV radiation. Goodness of fit and slope characteristics for Figure 5a are shown in Table 4.

**Table 4.** Goodness of fit and slope characteristics for Figure 5a.

R^2	Slope
0.9804	0.6530 ± 0.04126
0.9983	10.39 ± 0.1892
0.9970	28.64 ± 0.6978
0.9978	29.45 ± 0.6175

Figure 5b shows the intensity variation of the forward luminescent light for the different QD concentrations. These values were obtained using 11.9 mW incident UV radiation power. This figure depicts that the forward luminescent light production rate is increasing almost linearly up to the concentration of QD150 while after that point it tends to reach a plateau. Such performance is quite justified by taking into consideration effects such as self-absorption and Forster resonance energy transfer (FRET), which are of major importance. The relation between FRET and QD concentration has been studied extensively and is in accordance with our experimental results [41,42]. FRET involves the energy transfer between two neighbor chromophores. The donor chromophore at its excited state can transfer its excitation energy to the receptor chromophore via a non-radiative dipole–dipole coupling mechanism. Still, it is a prerequisite that the two chromophores must be in proximity, typically in a range of 3–10 nm. Generally, FRET efficiency increases with QD concentration until it saturates. The saturation level depends on the size of the chromophores, as well as on the distance between the donor and the receptor. In our case, it appears that the FRET saturation level was reached at the concentration of QD150, approximately. Self-absorption is a known drawback of quantum materials [43–45]. Most QDs have a partially overlapping absorption and emission spectrum. The extent of that overlapping defines the Stokes shift. Higher Stokes shifts denote less absorption and emission spectrum overlapping and, thus, less self-absorption effect. Moreover, an increase of the QD concentration means that there is a direct increase of the scattering centers in the material. Figure 5c demonstrates the amount of the incident UV radiation that passed through the compound films. UV radiation passed through only the QD25 film, by approximately 9%. QD100, QD150, and QD250 films were practically impermeable to UV radiation. The power of the transmitted UV radiation was not affected by the power increase of the incident UV radiation, as seen in Figure 5d. Furthermore, using the experimental configuration demonstrated in Figure 2b, the power of the reflected UV radiation and the power of the backward luminescent light were recorded.
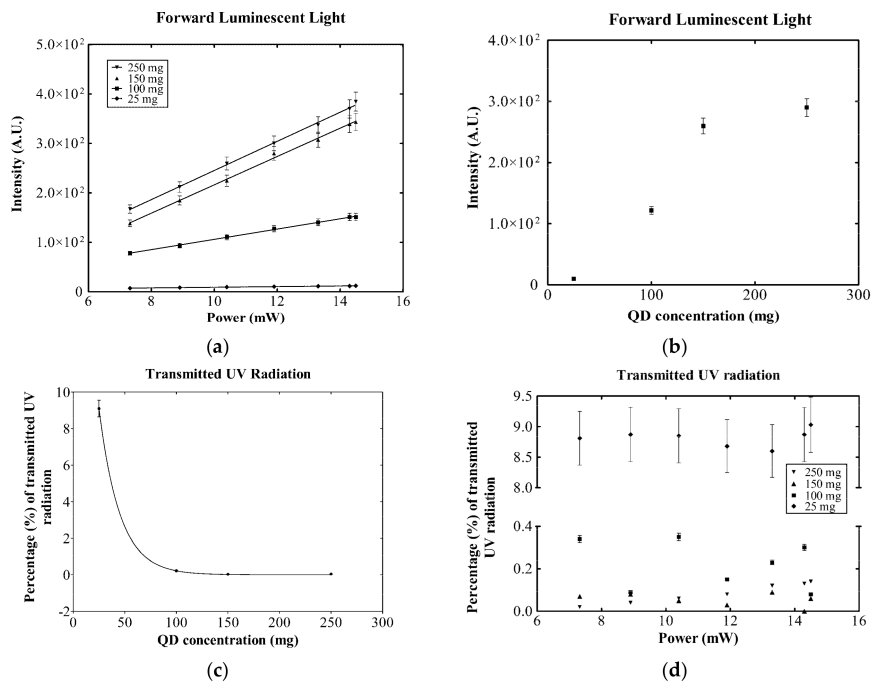
Figure 5. (**a**) The intensity variation of the forward luminescent light while increasing the power of the incident UV radiation; (**b**) the intensity variation of the forward luminescent light while changing the QD concentrations; (**c**) the percentage of the incident UV radiation that passed through the compound films for the four QD concentrations; and (**d**) the percentage of the UV radiation that passed through the compound films by increasing the power of the incident UV radiation.

As seen in Figure 6a, the intensity of the reflected UV radiation ranges from about 2% to approximately 6% of the incident UV radiation, as the quantum dot concentration ranges from 25 to 250 mg. Values for Figure 6a were obtained using 11.9 mW incident UV radiation power. The intensity of the reflected UV radiation increased up to the concentration of QD150 while after that point it remained virtually unchanged, indicating that the concentration of the QDs affects the composition of the reflective surface and, thus, the optical properties of the compound films, such as refractive index, back scattering, etc. [46,47]. Reflected UV radiation remains almost unaffected by the increase of the power of the incident UV radiation, Figure 6b.
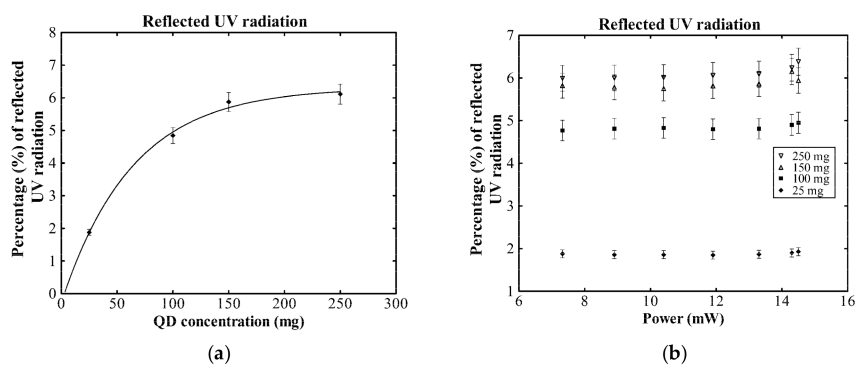

Figure 6. (**a**) The percentage of the reflected UV radiation by increasing the concentration of the QDs in the compound films and (**b**) the percentage of the reflected UV radiation by increasing the power of the incident UV radiation.

Figure 7 shows the backward luminescent performance of the four compound films with the increase of the power of the incident UV radiation, as well as the increase of the concentration of the

QDs. Values for Figure 7b were obtained using 11.9 mW incident UV radiation power. The backward luminescent light, as shown in Figure 7a,b, has almost the same response as the forward luminescent light in Figure 5a,b, respectively. Direct comparison between forward and backward luminescent light for the four QD samples shows that when the QD concentrations exceeded the concentration of QD100, the incident UV photons interacted only with the very first layers of QDs due to the high QD density, thus producing luminescence very close to the incident surface of the compound film. The latter is presented in Figure 8 where it is clearly seen that after the concentration of QD100 the dominant luminescence is reversed from forward to backward.
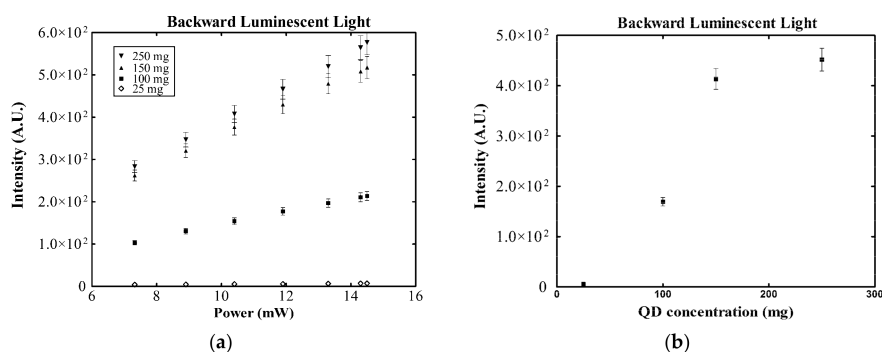
Figure 7. (**a**) The variation of the backward luminescent light by increasing the power of the incident UV radiation and (**b**) the variation of the backward luminescent light by increasing the concentration of the QDs in the compound films.
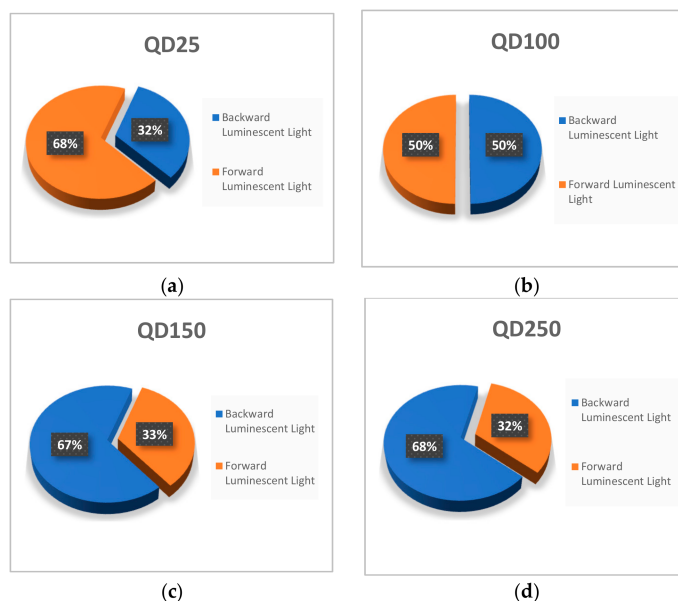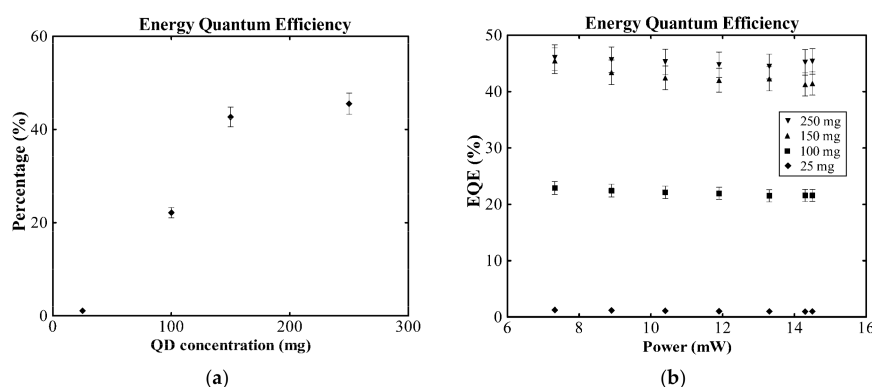

Figure 8. (**a**) The percentage of forward and backward luminescence light for the compound film with a QD concentration of QD25; (**b**) the percentage of forward and backward luminescence light for the compound film with a QD concentration of QD100; (**c**) the percentage of forward and backward luminescence light for the compound film with a QD concentration of QD150; and (**d**) the percentage of forward and backward luminescence light for the compound film with a QD concentration of QD250.

To accurately calculate the EQE of the compound films, the reflected UV radiation and the UV radiation that passed through the samples were subtracted from incident UV radiation since they did not contribute to the production of luminescence. The EQE reached a maximum of 45.52% with the QD250 sample as presented in Figure 9a. Beyond the concentration of QD150, EQE saturated as

a result of several previously described effects such as FRET, self-absorption, and scattering. EQE remained unaffected by the increase of the power of the incident UV radiation, Figure 9b.

Figure 9. (**a**) The variation of the energy quantum efficiency (EQE) by increasing the concentration of the QDs in the compound films and (**b**) the variation of EQE by increasing the power of the incident UV radiation.

4. Discussion

In this research, we present a simple method for the fabrication of QDs/PMMA films. Each step of the manufacturing procedure is described in detail. Forward and backward luminescent light showed a linear increase with the increase of the incident UV radiation. Forward luminescence light, as well as backward luminescent light, saturated when the concentration reached QD150. Both phenomena are explained with well-known mechanisms, such as self-absorption and FRET. It is worth noting that for the ZnCuInS/ZnS QDs the concentration of QD100 might be a marginal concentration, after which the dominant luminescence is reversed from forward to backward, even though more measurements around the concentration of QD100 could optimize the accuracy of that value. The latter is an essential parameter for the design of novel dual-mode imaging modalities such as hybrid UV–X-ray equipment or for in vivo imaging, as well as in microscopy [48–50]. This conclusion might also be of value for the design of non-medical applications such as light-emitting diodes (LEDs), displays, and photovoltaics.

The measurement of the reflected UV radiation revealed that the concentration of the QDs affects the optical properties of the compound films, such as refractive index, back scattering, etc. [46,47]. Fabrication of compound films with layers of different QD concentrations could lead to the minimization of the reflected UV radiation, thus increasing the amount of radiation that contributes to the production of luminescent light.

Furthermore, the EQE of the compound films was calculated when exposed to UV radiation. Transmitted UV radiation and reflected UV radiation were not taken into account for the calculation of the EQE since they do not contribute to luminescence. Due to experimental limitations, we only considered the forward and backward luminescence but not the lateral luminescence in order to calculate the EQE. Thus, it is expected that the actual EQE would be higher than 45.52%.

Homogeneity of the PMMA matrix and QD dispersion was evaluated by means of X-ray irradiation. Excellent PMMA homogeneity was achieved; however, the formation of QD clusters as a result of aggregations was also revealed. QD25, QD100, and QD150 developed a significant amount of QD clusters while QD250 performed much better due to the use of sonication. Excessive aggregation can lead to the formation of QD clusters, which behave like energy traps and can trigger several excitation energy transfer processes, such as FRET, due to short interparticle distances. Photoluminescence quenching and energy trapping due to energy migration in the QD lattice have been well described [51–54]. Photoluminescence quenching was not observed in our experiments, not even in QD100 and QD150, where strong QD aggregation was present. However, a photoluminescence plateau appeared with the QD250 sample, which exhibited minimum CV and QD aggregation. The latter may lead to the conclusion that even though QD clustering, due to increased QD concentration,

may play a role in luminescence efficiency, it might not be as significant as the non-radiative excitation energy transfer mechanisms. These mechanisms tend to be quite prominent in our experiments, and the observed plateau is attributed to them. The luminescence efficiency can be also affected by QD composition. During the fabrication phase of QDs, oxygen (O_2) pressure can also affect the defect formation and oxygen vacancies on the QD film properties [55,56]. Inhomogeneities in QD height, diameter, volume, and strain that usually appear in ensembles of QDs can also affect the luminescence efficiency [57]. The emission wavelength of QDs is directly linked to their quantum confinement, which is also directly affected by their shape and size. Theoretical studies have been carried out on how the electronic structure of InAs/GaAs QDs of different crystalline shapes and sizes can affect their optical properties [58,59]. In general, such inhomogeneities have an impact on the optical properties of QDs by broadening the full width at half maximum (FWHM) of the photoluminescence emission peak. A theoretical approach on how to control the broadening of FWHM of the photoluminescence emission peak has shown that intermixing can lead to the reduction of the linewidth of the photoluminescence peak [58].

Further optimization of the fabrication method is needed, including pre-polymerization of MMA, which could lead to minimization of QD clustering and better QD dispersion, as well as other parameters such as the sonication and steering duration, polymerization temperature, and the vacuum applied for the degassing process. Additionally, fabrication of QD/PMMA films with layers of different QD concentrations could minimize the reflected radiation and, thus, maximize the radiation contributed to luminescence.

Author Contributions: Conceptualization, G.S., I.V. and N.K.; methodology, G.S., C.M., I.V., N.K., G.S.P. and I.K.; software, G.S., I.S., N.K.; validation, G.S., C.F., A.B., N.K. and K.N.; formal analysis, G.S., C.M., N.K., G.S.P. and I.V.; investigation, G.S., C.M. , N.K., I.K., K.N. and I.V.; resources, K.N., C.F. and A.B.; data curation, G.S., C.M., I.K., G.F., I.S. and I.V.; writing—original draft preparation, G.S., N.K. and C.M.; writing—review and editing, I.K., G.S.P. and I.V.; visualization, G.S. and N.K.; supervision, I.V. and G.S.P.; project administration, G.S., K.N. and I.V. ; funding acquisition, C.F., G.S.P. and K.N.

Conflicts of Interest: The authors declare no conflict of interest.

References

1. Feng, Q.; Wei, W.; Zhang, B.; Wang, H.; Wang, J.; Cong, H.; Wang, T.; Zhang, J. O-Band and C/L-Band III-V quantum dot lasers monolithically grown on ge and si substrate. *Appl. Sci.* **2019**, *9*, 385. [CrossRef]

2. Qin, Y.; Feng, X.; Liu, Y. Nonlinear refractive index in rectangular graphene quantum dots. *Appl. Sci.* **2019**, *9*, 325. [CrossRef]

3. Ganesan, A.A.; Houtepen, A.J.; Crisp, R.W. Quantum dot solar cells: Small beginnings have large impacts. *Appl. Sci.* **2018**, *8*, 1867. [CrossRef]

4. Zych, E.; Meijerink, A.; Doneg, C.d.M. Quantum efficiency of europium emission from nanocrystalline powders of Lu_2O_3:Eu. *J. Phys. Condens. Matter* **2003**, *15*, 5145–5155. [CrossRef]

5. Kim, S.; Park, J.; Kang, S.; Cha, B.; Cho, S.; Shin, J.; Son, D.; Nam, S. Investigation of the imaging characteristics of the Gd_2O_3: Eu nanophosphor for high-resolution digital X-ray imaging system. *Nucl. Instrum. Methods Phys. Res. Sect. A Accel. Spectrom. Detect. Assoc. Equip.* **2007**, *576*, 70–74. [CrossRef]

6. Konstantatos, G.; Clifford, J.; Levina, L.; Sargent, E.H. Sensitive solution-processed visible-wavelength photodetectors. *Nat. Photonics* **2007**, *1*, 531–534. [CrossRef]

7. Konstantatos, G.; Sargent, E.H. Colloidal quantum dot photodetectors. *Infrared Phys. Technol.* **2011**, *54*, 278–282. [CrossRef]

8. Del Sordo, S.; Abbene, L.; Caroli, E.; Mancini, A.M.; Zappettini, A.; Ubertini, P. Progress in the development of CdTe and CdZnTe semiconductor radiation detectors for astrophysical and medical applications. *Sensors* **2009**, *9*, 3491–3526. [CrossRef]

9. Rauch, T.; Böberl, M.; Tedde, S.F.; Fürst, J.; Kovalenko, M.V.; Hesser, G.; Lemmer, U.; Heiss, W.; Hayden, O. Near-infrared imaging with quantum-dot-sensitized organic photodiodes. *Nat. Photonics* **2009**, *3*, 332–336. [CrossRef]

10. Stodilka, R.Z.; Carson, J.J.L.; Yu, K.; Zaman, M.B.; Li, C.; Wilkinson, D. Optical Degradation of CdSe/ZnS Quantum Dots upon Gamma-Ray Irradiation. *J. Phys. Chem. C* **2009**, *113*, 2580–2585. [CrossRef]

11. Baharin, R.; Hobson, P.R.; Smith, D.R. Simulation of MeV electron energy deposition in CdS quantum dots absorbed in silicate glass for radiation dosimetry. *J. Phys. Conf. Ser.* **2010**, *245*, 012007. [CrossRef]

12. Öberg, V.A.; Zhang, X.; Johansson, M.B.; Johansson, E.M.J. Solution-processed environmentally friendly Ag_2S colloidal quantum dot solar cells with broad spectral absorption. *Appl. Sci.* **2017**, *7*, 1020. [CrossRef]

13. Chan, W.C. Quantum Dot Bioconjugates for Ultrasensitive Nonisotopic Detection. *Science* **1998**, *281*, 2016–2018. [CrossRef] [PubMed]

14. Ballou, B.; Lagerholm, B.C.; Ernst, L.A.; Bruchez, M.P.; Waggoner, A.S. Noninvasive imaging of quantum dots in mice. *Bioconjug. Chem.* **2004**, *15*, 79–86. [CrossRef]

15. Jamieson, T.; Bakhshi, R.; Petrova, D.; Pocock, R.; Imani, M.; Seifalian, A.M. Biological applications of quantum dots. *Biomaterials* **2007**, *28*, 4717–4732. [CrossRef]

16. Yu, W.W.; Chang, E.; Drezek, R.; Colvin, V.L. Water-soluble quantum dots for biomedical applications. *Biochem. Biophys. Res. Commun.* **2006**, *348*, 781–786. [CrossRef]

17. Son, D.I.; Kwon, B.W.; Park, D.H.; Seo, W.-S.; Yi, Y.; Angadi, B.; Lee, C.-L.; Choi, W.K. Emissive ZnO–graphene quantum dots for white-light-emitting diodes. *Nat. Nanotechnol.* **2012**, *7*, 465–471. [CrossRef]

18. Lawrence, W.G.; Thacker, S.; Palamakumbura, S.; Riley, K.J.; Nagarkar, V.V. Quantum dot-organic polymer composite materials for radiation detection and imaging. *IEEE Trans. Nucl. Sci.* **2012**, *59*, 215–221. [CrossRef]

19. Wu, T.; Sher, C.-W.; Lin, Y.; Lee, C.-F.; Liang, S.; Lu, Y.; Huang Chen, S.-W.; Guo, W.; Kuo, H.-C.; Chen, Z. Mini-LED and Micro-LED: Promising candidates for the next generation display technology. *Appl. Sci.* **2018**, *8*, 1557. [CrossRef]

20. Nikolopoulos, D.; Valais, I.; Michail, C.; Bakas, A.; Fountzoula, C.; Cantzos, D.; Bhattacharyya, D.; Sianoudis, I.; Fountos, G.; Yannakopoulos, P.; et al. Radioluminescence properties of the CdSe/ZnS Quantum Dot nanocrystals with analysis of long-memory trends. *Radiat. Meas.* **2016**, *92*, 19–31. [CrossRef]

21. Fiaczyk, K.; Zych, E. On peculiarities of Eu^{3+} and Eu^{2+} luminescence in Sr_2GeO_4 host. *RSC Adv.* **2016**, *6*, 91836. [CrossRef]

22. Zeler, J.; Cybinska, J.; Zych, E. A new photoluminescent feature in $LuPO_4$: Eu thermoluminescent sintered materials. *RSC Adv.* **2016**, *6*, 57920. [CrossRef]

23. Public Health England. Cadmium: Health Effects, Incident Management and Toxicology. Information on Cadmium, for Responding to Chemical Incidents. Published 1 July 2014, Last updated 25 October 2016. Available online: https://www.gov.uk/government/publications/cadmium-properties-incident-management-and-toxicology (accessed on 10 April 2019).

24. Valais, I.; Kandarakis, I.; Nikolopoulos, D.; Michail, C.; David, S.; Loudos, G.; Cavouras, D.; Panayiotakis, G. Luminescence properties of $(Lu,Y)_2SiO_5$:Ce and Gd_2SiO_5:Ce single crystal scintillators under X-ray excitation for use in medical imaging systems. *IEEE Trans. Nucl. Sci.* **2007**, *54*, 11–18. [CrossRef]

25. Michail, C.; Fountos, G.; Liaparinos, P.; Kalyvas, N.; Valais, I.; Kandarakis, I.; Panayiotakis, G. Light emission efficiency and imaging performance of Gd_2O_2S:Eu powder scintillator under X-ray Radiography conditions. *Med. Phys.* **2010**, *37*, 3694–3703. [CrossRef] [PubMed]

26. Valais, I.; Michail, C.; David, S.; Liaparinos, P.; Fountos, G.; Paschalis, T.; Kandarakis, I.; Panayiotakis, G. Comparative Investigation of Ce^{3+} doped Scintillators in a wide Range of Photon Energies covering X-ray CT, Nuclear Medicine and Megavoltage Radiation Therapy Portal Imaging applications. *IEEE Trans. Nucl. Sci.* **2010**, *57*, 3–7. [CrossRef]

27. Michail, C.; Karpetas, G.; Kalyvas, N.; Valais, I.; Kandarakis, I.; Agavanakis, K.; Panayiotakis, G.; Fountos, G. Information Capacity of Positron Emission Tomography Scanners. *Crystals* **2018**, *8*, 459. [CrossRef]

28. Michail, C.; Valais, I.; Fountos, G.; Bakas, A.; Fountzoula, C.; Kalyvas, N.; Karabotsos, A.; Sianoudis, I.; Kandarakis, I. Luminescence Efficiency of Calcium Tungstate ($CaWO_4$) under X-ray radiation: Comparison with Gd_2O_2S:Tb. *Measurement* **2018**, *120*, 213–220. [CrossRef]

29. Dong, X.; Xu, J.; Shi, S.; Zhang, X.; Li, L.; Yin, S. Electroluminescence from ZnCuInS/ZnS quantum dots/poly(9-vinylcarbazole) multilayer films with different thicknesses of quantum dot layer. *J. Phys. Chem. Solids* **2017**, *104*, 133–138. [CrossRef]

30. Seferis, I.E.; Zeler, J.; Michail, C.; Valais, I.; Fountos, G.; Kalyvas, N.; Bakas, A.; Kandarakis, I.; Zych, E. On the response of semitransparent nanoparticulated films of LuPO$_4$:Eu in poly-energetic X-ray imaging applications. *Appl. Phys. A* **2016**, *122*, 526. [CrossRef]

31. Seferis, I.E.; Zeler, J.; Michail, C.; David, S.; Valais, I.; Fountos, G.; Kalyvas, N.; Bakas, A.; Kandarakis, I.; Zych, E.; et al. Grains size and shape dependence of luminescence efficiency of Lu$_2$O$_3$:Eu thin screens. *Results Phys.* **2017**, *7*, 980–981. [CrossRef]

32. Seferis, I.E.; Michail, C.; Zeler, J.; Kalyvas, N.; Valais, I.; Fountos, G.; Bakas, A.; Kandarakis, I.; Zych, E.; Panayiotakis, G.S. Detective quantum efficiency (DQE) of high X-ray absorption Lu$_2$O$_3$:Eu thin screens: The role of shape and size of nano- and micro-grains. *Appl. Phys. A* **2018**, *124*. [CrossRef]

33. Allcock, H.R.; Bender, J.D.; Chang, Y.; McKenzie, M.; Fone, M.M. Controlled Refractive Index Polymers: Polyphosphazenes with Chlorinated- and Fluorinated-, Aryloxy- and Alkoxy- Side-Groups. *Chem. Mater.* **2003**, *15*, 473–477. [CrossRef]

34. Balamurugan, A.; Kannan, S.; Selvaraj, V.; Rajeswari, S. Development and Spectral Characterization of Poly (Methyl Methacrylate)/Hydroxyapatite Composite for Biomedical Applications. *Trends Biomater. Artif. Organs* **2004**, *18*, 41–45.

35. Valais, I.; Michail, C.; Fountzoula, C.; Tseles, D.; Yannakopoulos, P.; Nikolopoulos, D.; Bakas, A.; Fountos, G.; Saatsakis, G.; Sianoudis, I.; et al. On the response of alloyed ZnCdSeS quantum dot films. *Results Phys.* **2017**, *7*, 1734–1736. [CrossRef]

36. Thomson, L.A.; Law, F.C.; James, K.H.; Matthew, C.A.; Rushton, N. Biocompatibility of particulate polymethylmethacrylate bone cements: A comparative study in vitro and in vivo. *Biomaterials* **1992**, *13*, 811–818. [CrossRef]

37. Hollick, E.J.; Spalton, D.J.; Ursell, P.G.; Pande, M.V.; Barman, S.A.; Boyce, J.F.; Tilling, K. The effect of polymethylmethacrylate, silicone, and polyacrylic intraocular lenses on posterior capsular opacification 3 years after cataract surgery. *Ophthalmology* **1999**, *106*, 49–55. [CrossRef]

38. Gautam, R.; Singh, R.D.; Sharma, V.P.; Siddhartha, R.; Chand, P.; Kumar, R. Biocompatibility of polymethylmethacrylate resins used in dentistry. *J. Biomed. Mater. Res. Part B Appl. Biomater.* **2012**, *100B*, 1444–1450. [CrossRef]

39. Huettig, F.; Prutscher, A.; Goldammer, C.; Kreutzer, C.A.; Weber, H. First clinical experiences with CAD/CAM-fabricated PMMA-based fixed dental prostheses as long-term temporaries. *Clin. Oral Investig.* **2016**, *20*, 161–168. [CrossRef]

40. Kong, L.B.; Huang, Y.Z.; Que, W.X.; Zhang, T.S.; Li, S.; Zhang, J.; Dong, Z.L.; Tang, D.Y. *Transparent Ceramics (Topics in Mining, Metallurgy and Materials Engineering)*; Springer International Publishing: Cham, Switzerland, 2015; ISBN 978-3-319-18955-0.

41. Clapp, A.R.; Medintz, I.L.; Mattoussi, H. Förster resonance energy transfer investigations using quantum-dot fluorophores. *ChemPhysChem* **2006**, *7*, 47–57. [CrossRef]

42. Litvin, A.P.; Ushakova, E.V.; Parfenov, P.S.; Cherevkov, S.A.; Fedorov, A.V.; Baranov, A.V. Förster resonant energy transfer in lead sulfide QD assemblies. In Proceedings of the SPIE Photonics Europe, Brussels, Belgium, 14–17 April 2014; Volume 9126, p. 912626.

43. Roncali, J.; Garnier, F. Photon-transport properties of luminescent solar concentrators: Analysis and optimization. *Appl. Opt.* **1984**, *23*, 2809–2817. [CrossRef]

44. Krumer, Z.; Pera, S.J.; van Dijk-Moes, R.J.A.; Zhao, Y.; de Brouwer, A.F.P.; Groeneveld, E.; van Sark, W.G.J.H.M.; Schropp, R.E.I.; de Mello Donegá, C. Tackling self-absorption in luminescent solar concentrators with type-II colloidal quantum dots. *Sol. Energy Mater. Sol. Cells* **2013**, *111*, 57–65. [CrossRef]

45. Krumer, Z.; van Sark, W.G.J.H.M.; Schropp, R.E.I.; de Mello Donegá, C. Compensation of self-absorption losses in luminescent solar concentrators by increasing luminophore concentration. *Sol. Energy Mater. Sol. Cells* **2017**, *167*, 133–139. [CrossRef]

46. Kumar, V.B.; Sahu, A.K.; Mohsin, A.S.M.; Li, X.; Gedanken, A. Refractive-Index Tuning of Highly Fluorescent Carbon Dots. *ACS Appl. Mater. Interf.* **2017**, *9*, 28930–28938. [CrossRef] [PubMed]

47. Chen, J.; Chen, X.; Xu, R.; Zhu, Y.; Shi, Y.; Zhu, X. Refractive index of aqueous solution of CdTe quantum dots. *Opt. Commun.* **2008**, *281*, 3578–3580. [CrossRef]

48. Giepmans, B.N.G.; Deerinck, T.J.; Smarr, B.L.; Jones, Y.Z.; Ellisman, M.H. Correlated light and electron microscopic imaging of multiple endogenous proteins using Quantum dots. *Nat. Methods* **2005**, *2*, 743–749. [CrossRef] [PubMed]

49. Luo, T.; Huang, P.; Gao, G.; Shen, G.; Fu, S.; Cui, D.; Zhou, C.; Ren, Q. Mesoporous silica-coated gold nanorods with embedded indocyanine green for dual mode X-ray CT and NIR fluorescence imaging. *Opt. Express* **2011**, *19*, 17030–17039. [CrossRef] [PubMed]

50. Michalet, X. Quantum Dots for Live Cells, in Vivo Imaging, and Diagnostics. *Science* **2005**, *307*, 538–544. [CrossRef] [PubMed]

51. Martín-García, B.; Paulo, P.M.R.; Costa, S.M.B.; Velázquez, M.M. Photoluminescence dynamics of CdSe QD/Polymer langmuir–blodgett thin films: morphology effects. *J. Phys. Chem. C* **2013**, *117*, 14787–14795. [CrossRef]

52. Alejo, T.; Paulo, P.M.R.; Merchán, M.D.; Garcia-Fernandez, E.; Costa, S.M.B.; Velázquez, M.M. Influence of 3D aggregation on the photoluminescence dynamics of CdSe quantum dot films. *J. Lumin.* **2017**, *183*, 113–120. [CrossRef]

53. Liu, J.; Yang, X.; Wang, K.; He, X.; Wang, Q.; Huang, J.; Liu, Y. Aggregation control of quantum dots through ion-mediated hydrogen bonding shielding. *ACS Nano* **2012**, *6*, 4973–4983. [CrossRef] [PubMed]

54. Matvienko, O.O.; Savin, Y.N.; Kryzhanovska, A.S.; Vovk, O.M.; Dobrotvorska, M.V.; Pogorelova, N.V.; Vashchenko, V.V. Dispersion and aggregation of quantum dots in polymer–inorganic hybrid films. *Thin Solid Films* **2013**, *537*, 226–230. [CrossRef]

55. Gondoni, P.; Ghidelli, M.; Di Fonzo, F.; Russo, V.; Bruno, P.; Martí-Rujas, J.; Bottani, C.E.; Li Bassi, A.; Casari, C.S. Structural and functional properties of Al:ZnO thin films grown by Pulsed Laser Deposition at room temperature. *Thin Solid Films* **2012**, *520*, 4707–4711. [CrossRef]

56. Gondoni, P.; Ghidelli, M.; Di Fonzo, F.; Carminati, M.; Russo, V.; Li Bassi, A.; Casari, C.S. Structure-dependent optical and electrical transport properties of nanostructured Al-doped ZnO. *Nanotechnology* **2012**, *23*, 365706. [CrossRef] [PubMed]

57. Perret, N.; Morris, D.; Franchomme-Fossé, L.; Côté, R.; Fafard, S.; Aimez, V.; Beauvais, J. Origin of the inhomogenous broadening and alloy intermixing in InAs/GaAs self-assembled quantum dots. *Phys. Rev. B* **2000**, *62*, 5092–5099. [CrossRef]

58. Ngo, C.Y.; Yoon, S.F.; Fan, W.J.; Chua, S.J. Effects of size and shape on electronic states of quantum dots. *Phys. Rev. B* **2006**, *74*, 245331. [CrossRef]

59. Xie, H.; Prioli, R.; Torelly, G.; Liu, H.; Fischer, A.M.; Jakomin, R.; Mourão, R.; Kawabata, R.; Pires, M.P.; Souza, P.L.; et al. Correlation between size distribution and luminescence properties of spool-shaped InAs quantum dots. *Semicond. Sci. Technol.* **2017**, *32*, 055013. [CrossRef]